Operando nuclear magnetic resonance spectroscopy: Detection of the onset of metallic lithium deposition on graphite at low temperature and fast charge in a full Li-ion battery

Ludivine Afonso de Araujo, Vincent Sarou-Kanian, David Sicsic, Michael Deschamps, Elodie Salager

Operando Nuclear Magnetic Resonance spectroscopy: detection of the onset of metallic lithium deposition on graphite at low temperature and fast charge in a full Li-ion battery

Ludivine Afonso de Araujo[1,2,3], Vincent Sarou-Kanian,[1,3] David Sicsic[2,3], Michael Deschamps[1,3], Elodie Salager*[1,3]

[1]CNRS, CEMHTI UPR3079, Université d'Orléans, 1D Avenue de la Recherche Scientifique, F-45071 Orléans Cedex 2, France
[2]Renault SAS, Technocentre Renault, 1 Avenue du Golf, F-78288 Guyancourt, France
[3]Réseau sur le Stockage Électrochimique de l'Énergie (RS2E), CNRS FR3459, 33 Rue Saint Leu, F-80039 Amiens Cedex, France

*E-mail: elodie.salager@cnrs-orleans.fr

Key words: *operando* NMR, *in situ* NMR, Li-ion battery, Lithium plating, graphite, full cell, low temperature, 7-lithium, fast charge, pressure

Abstract

Lithium-ion batteries are at the core of the democratisation of electric transportation and portative electronic devices. However, fast and/or low temperature charge induce performance loss, mainly through lithium plating, a degrading mechanism. In this report, ^{7}Li *operando* Nuclear Magnetic Resonance spectroscopy is used to detect the onset of metastable lithium deposits in an NMC622/graphite cell at 0°C and fast charge. An *operando* setup, compatible with low temperatures, was developed with special attention to the pressure applied on the electrodes/separator stack and noise reduction to enable early detection and good time-resolution. Direct detection of metallic lithium enables drawing correlations between lithium plating and electrochemical data.

1 Introduction

Lithium-ion batteries (LiBs) are ubiquitous in our daily lives, from small portative devices to electrical vehicles. Societal demand urges reaching always faster charge (time savings), while retaining the autonomy of the battery (stored capacity) in the long term. Capacity loss in batteries is a multifactorial issue, with a strong interplay between environmental factors - especially temperature - and usage. Despite numerous studies the precise modelling of the state of health of a battery without exact knowledge of its history is extremely challenging [1–5].

Among the multiple degrading phenomena, lithium plating (reduction of Li^+ ions into metallic lithium) is observed as a side-reaction competing with the normal redox behaviour of the negative graphite electrode in the battery [6]. Electroplating of Li on the surface of the graphite electrode occurs, rather than reductive insertion in graphite, when the potential is locally lower than that of the Li^+/Li redox couple due to kinetic limitations. This highly reducing

metallic lithium may react irreversibly with the electrolyte components and the current collectors, hence reducing the energy available on discharge. An additional issue is the spatially inhomogeneous deposition of lithium (dendrites), which results in micro short-circuits detrimental for the capacity retention of the battery and, in extreme cases, battery failure.
Fast charge and charge to full capacity favour this side reaction, and conservative safety margins are currently taken in the charging protocols - at the expense of autonomy and charging times [7–10]. Better tuning of the charging protocols, while preserving safety, requires a better knowledge and understanding of the onset conditions for Li plating.

Deposition of metallic lithium in batteries has been intensively researched and many approaches have been proposed [11,12]. They were classified in various ways such as direct or indirect, local or global, *ex situ* or *in situ*, etc…. *Operando* characterization, i.e. the characterization of the entire battery device while it is charging (or discharging), is highly desirable due to the high reactivity of metallic lithium [13,14]. Among all the available *operando* techniques, ^{7}Li *operando* Nuclear Magnetic Resonance (NMR) spectroscopy appears as a direct and global technique, well-suited to the task of detecting Li plating [15–21]. The specific Knight shift of metallic Li, signature of its metallicity, is well-resolved from the other lithiated components of the battery even in static conditions (240-270 ppm range) as already seen in the early days of *in situ* NMR with a metallic Li counter electrode [22–25].

Detecting lithium deposition on the graphite electrodes, as a degrading phenomenon, is more challenging owing to the lower quantities. The early ^{7}Li NMR analyses of plating on graphite were reported on half cells, with metallic Li as the counter electrode [26–28].
Artefacts can arise from the use of a metallic Li counter electrode rather than a positive electrode. Only a few reports focused on Li plating on graphite in batteries with a realistic positive electrode. Gotoh *et al* [29,30] were the first to characterize full cells with graphite and $LiCoO_2$ electrodes to analyse the evolution in open circuit and overcharge conditions. Kayser developed another setup for long-term studies (100 cycles) on the same system in 2018 [28]. Goward and Balcom used a smart design with a home-made flat electrochemical cell (cartridge) slid into a parallel plate resonator [31] to observe Li plating at high charging rates in a cell assembled with graphite and $LiNi_{0.6}Mn_{0.2}Co_{0.2}O_2$ (NMC622) electrodes harvested from an electric vehicle battery cell. [32,33].
The effect of low temperature was less studied for full cells, with only two reports to the best of our knowledge. Arai *et al* [34] characterized full cells ($LiCoO_2$/graphite) at different temperatures (5°C, 0°C, -5°C) and observed increased plated lithium with decreasing temperature. Märker *et al* [35] observed the same effect on $LiNi_{0.8}Mn_{0.1}Co_{0.1}O_2$ (NMC811)/graphite full cells for temperatures ranging from -20°C to 25°C.

Herein, we report the study on $LiNi_{0.6}Mn_{0.2}Co_{0.2}O_2$ (NMC622)/graphite full cells at low temperature and fast charging rates for the first time, to the best of our knowledge. We chose to focus on the early detection of the onset of Li plating, rather than quantifying precisely the amount of metallic Li. The transition from surface-dependence [36] of the NMR signal to volume-dependence [25] is indeed difficult to predict in real time without prior knowledge of the morphology [37].

Applied or internal pressure on the battery stacked electrodes is another important factor that limits the onset of the Li deposit and impacts its morphology [38]. Smart approaches enabled the measurement of an indirect "fingerprint" of cells with commercial casings to identify faulty batteries [39–41], but the chemical information was lost. Recently, Walder et al. reported the measurement, with a hairpin lock resonator and on a stainless-steel coin cell, of a decent signal containing chemical information shift information about the electrodes [42]. This promising approach should be further explored in the future.
Apart from these reports, the stainless steel container was usually replaced for *operando* NMR with home-made aluminized plastic pouches or with purely plastic cell containers, as conductive parts attenuate and/or distort the NMR signal [15–20,43].

The electrochemical plastic cell developed at CEMHTI [44], is ideal for better control of the pressure on the battery core compared to home-made pouches or capsules. The top current collector is screwed towards the bottom current collector in a Kel-F homemade electrochemical cell container. It is similar to the "Swagelok battery container" commonly used in lab-scale studies, with electrodes stacked as in a coin cell. A similar design had been reported in literature a year earlier to perform stray-field imaging [45].

We worked on developing an operando NMR setup compatible with our plastic cell container, which could be operated at low temperatures. The small dimensions of the electrodes combined with good pressure result in low amounts of plated Li. We therefore optimized the electrical connections to lower the noise induced on the NMR measurements and we worked on the processing to enable the detection of Li plating as early as possible, even with noisy data. We demonstrate its efficiency with the detection of metallic deposition by ^{7}Li *operando* NMR in a full cell, using commercial NMC622 ($LiNi_{0.6}Mn_{0.2}Co_{0.2}O_2$) and graphite industry-grade electrodes for the first time at low temperature and fast charging rates.

2 Experimental details & Methods

2.1 *Operando* NMR setup

The general setup of an *in situ* measurement is described in **Figure 1**. The electrochemical cell (1) is located in the NMR probe at the magnetic centre of the NMR magnet.
It is connected with electric cables (4,6) to a galvanostat-potentiostat (7) that controls current/voltage for charging and discharging the cell, while the probe (3) including the resonator (2) are used for NMR spectroscopy.
Current running in the electric cables interfere with those in the vicinity of the NMR resonator. The resulting parasitic signals in the NMR measurement and/or for the electrochemical measurement are usually mitigated by the use of a low-pass filter (5) on the electrochemical cables.

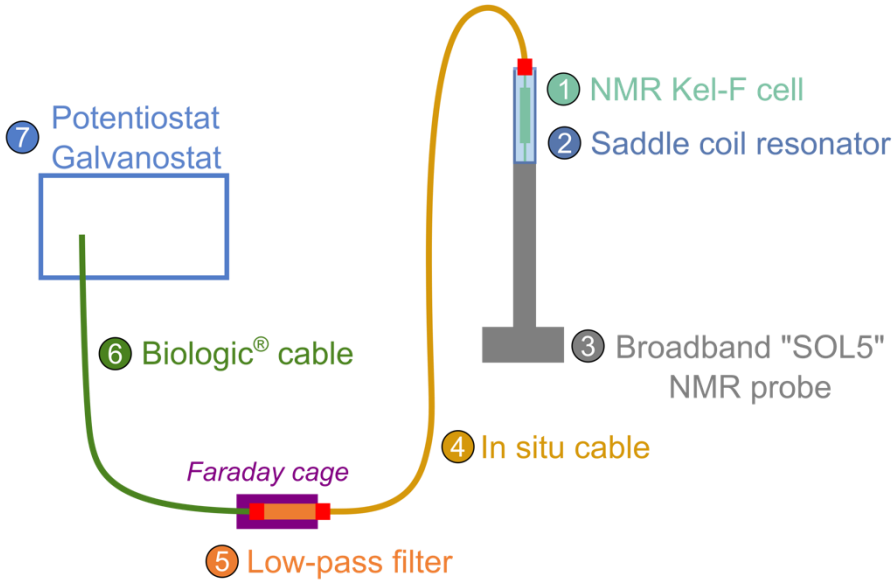

Figure 1 : Schematics of the *operando* NMR setup

2.2 Battery materials

Data provided by the supplier for the commercial-grade one-sided NMC622 ($LiNi_{0.6}Mn_{0.2}Co_{0.2}O_2$) and graphite electrodes are presented in Table 1. Approximatively 5 mm diameter disks were punched in the electrode foils and dried at 120°C overnight under vacuum. A 6 mm diameter separator (200 µm thick glass fiber, Whatman GF/D) and the homemade Kel-F electrochemical casing are dried at 60°C before assembly and activation in an argon-filled glovebox. The electrolyte is a 1 mol.L^{-1} solution of $LiPF_6$ dissolved in 1:1%v ethylene carbonate-dimethyl carbonate (Solvionics). The cell is set to charge within 4 hours after activation by the liquid electrolyte.

In the battery community, the charge that can be stored in the electrode is traditionally given per surface unit (mA·h/cm^2) and named "areal capacity". As a reminder 1 A·h=3600 A·s= 3600 C. The values from the provider are indicated in Table 1. They are slightly lower than the purely theoretical capacities as they take into account the loss of capacity in the initial "formation steps" (four first cycles of charge-discharge) and the potential restraints on the voltage window.

Electrode	Thickness	Active material content	Coating areal density ($d_{Supplier,L}$)	Areal capacity ($C_{Supplier,S}$)
NMC 622	85 µm	90%	24.45 mg/cm²	3.52 mA·h/cm²
Graphite	85 µm	96%	11.67 mg/cm²	3.92 mA·h/cm²

Table 1: Supplier information for the electrodes.

As the punching process is far from perfect, the real area of the electrodes was obtained by weighing the ~5 mm-disks after punching and assuming no variation in the thickness of the

deposit (surfaces of 0.213 and 0.194 cm^2 respectively, for the positive and the negative electrode). The negative to positive capacity ratio (N/P) was obtained using the expected capacities, taking into account the exact areas. For the cell reported in this study, the expected capacities are 0.751 mAh for the positive and 0.759 mAh for the negative electrode and result in a N/P ratio of 1.01. This ratio should be higher than 1 in full cells to avoid overlithiation of graphite.

2.3 Electrochemical cell casing

The electrochemical core (electrode disks separated by a glass-fiber separator) is placed in the home-made Kel-F casing developed at CEMHTI [44]. As shown in **Figure *2***, the outer diameter of the casing is 10 mm to fit inside saddle coil resonators designed for 10mm NMR tubes. Threading of the top part controls the pressure applied to the battery core and o-rings ensure air-tightness. The 5.5 mm-diameter copper and aluminium current collectors are 2mm-thick for rigidity and they are embedded into the Kel-F guide to ensure uniform pressure on the electrodes. The collector wires are connected to the *in situ* cable for the charge and discharge.

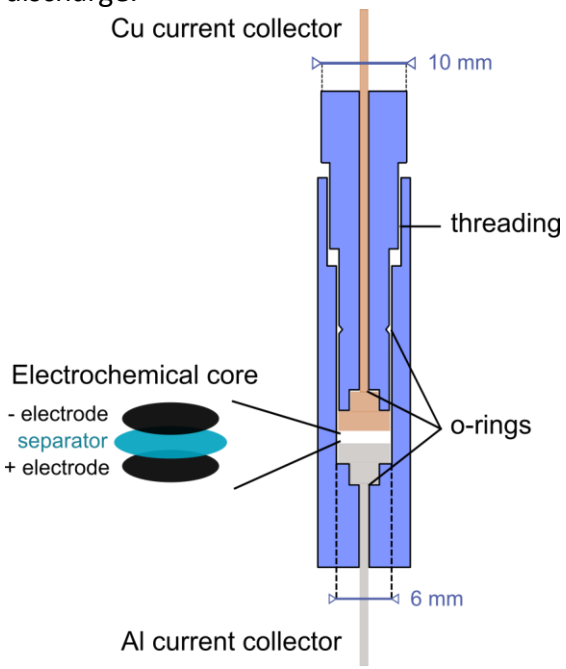

Figure 2 Schematics of our Kel-F battery casing for *operando* NMR

2.4 NMR probe modifications

The electrodes are deposited on metallic foils acting as current collectors. As conductors repel magnetic fields perpendicular to their surface (shielding), the orientation of the electrodes should be parallel to the RF excitation field [28,46]. The cell geometry and available space in the probehead therefore constrain the choice of the resonator.

In the literature [16–21] two types of cell geometries were developed: 1/ rectangular electrodes in pouch [23,24,29] or capsule cells [16,31,47] and 2/ disc electrodes in Swagelok-type containers [44,45,26,28]. The cell geometry constraints the resonator type to fit inside

the probe: geometries#1 require a longitudinal resonator (such as solenoids or parallel plates), while for geometries#2 transversal resonators should be used (e.g. saddle coils) [48].

For space reasons our battery container must be positioned vertically in the probehead and we are therefore constrained to use a transversal resonator. In previous studies [44,49–51], we used a commercial saddle coil in a modified diff50 probe from Bruker to allow the passage of the electrochemical cable through the body of the probe. The gradient coil and water-cooling system of this probe would be too sensitive for measurements at very low temperature, so we used a more robust Bruker single channel broadband static probe (SOL5), such as those typically used for pouch-cell *in situ* NMR.
The SOL5 probe was further modified to use our pressure-controlled cell by removing the commercial solenoid coil and its top cover, which were replaced with an in-house designed holder for a commercial saddle coil (1 cm diameter). This approach is closest to Kayser's design [28], which used a home-made saddle coil to study plating at room temperature on a graphite//Li electrochemical cell.

Figure 3a shows the coil and cell holder, which also helps for the electric connections for charge and discharge. The saddle coil is connected to the electronic circuit of the SOL5 probe. Low temperature is reached with a flow of cold nitrogen gas sent to the cell through the quartz dewar running accross the probe. The shape of the holder guides the flow towards the cell.
In **Figure 3**b, a cell is connected with the positive electrode on top connected to a brass screw on the right. The cell negative electrode is connected to the metallic cover of the probe acting as ground by clamping connections. A short description of the connexions is detailed in supplementary information (Figure S1 in SI).
The brass screws connect to the *in situ* cable for charging the cell, labelled (4) in Figure 1. As little space remains inside the probe, the *in situ* cable is connected from the top of the magnet. In this configuration the connections between the *in situ* cable and the cell are fragile and can easily be pulled out when installing the probe in the magnet. The probe cover was adapted with a customized polypropylene cable holder to hold the *in situ* electrical cable and protect the cell connections (Figure S1 in SI).

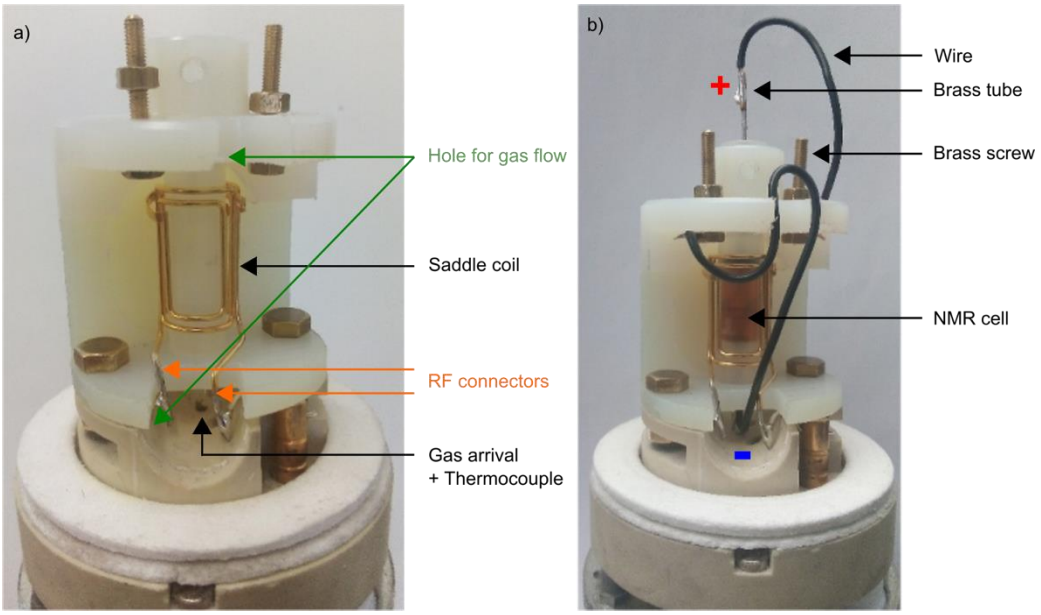

Figure 3 : (a) Saddle coil and its holder on the SOL5 probe, b) Setup and connections with our NMR cell.

2.5 Electrochemical connections and noise reduction

The electrochemical circuit connects the electrochemical cell (1 in Figure 1) to the galvanostat (7 in Figure 1). All *in situ* designs typically include a low-pass filter to reduce interferences between the constant current running in the battery and the RF current running in the NMR spectrometer. This is perfectly efficient to avoid disturbance by the RF pulses of the electrical charge of the battery. We noticed however that RF parasitic signal propagated to the NMR resonator through the electrochemical chain. This additional signal can preclude the detection of the interesting signal as shown in Figure 4a.

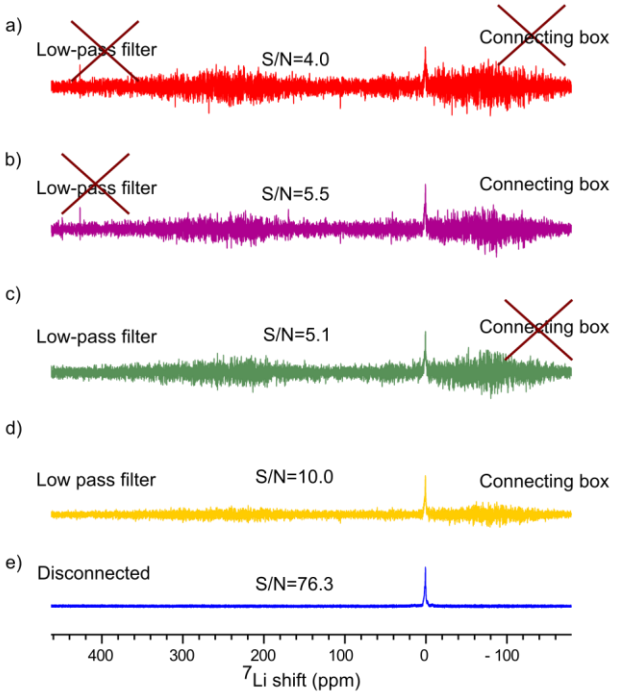

Figure 4: In situ ^{7}Li NMR spectra for the pristine cell with the *in situ* cable connected to the galvanostat with (a) no connecting box and no low-pass filter, (b) connecting box only, (c) low-pass folder only and (d) connecting box and low-pass filter. The spectrum of the disconnected cell is shown in (e). The signal-to-noise ratio (S/N) was determined using the SINO command in Topspin (noise region: [106;450] ppm; signal region: [-10;13] ppm).

Appropriate shielding and grounding of the galvanostat cable and *in situ* cable was crucial to limit the perturbations in the NMR detection. The cable layout also played a role on the amount of noise pickup.

Our setup uses the commercial galvanostat cable (6 in Figure 1) connected to a 1.9 MHz low-pass filter (5 in Figure 1, supplier Mini-Circuits®), then to an *in situ* cable (4 in Figure 1) running through the magnet bore to connect to the electrochemical cell. We used an HDMI cable, with a global aluminium foil and a global braiding. Wires shielded by an extra aluminium foil inside the HDMI sheath were used to transport current to the current collectors. Finally, we designed a connecting box (Figure S1) to change quickly the configuration of the incoming galvanostat connections. It also enables grounding the braid of the *in situ* and the galvanostat

cable while acting as a “Faraday cage” for the less-shielded home-made connections. Figure 4 shows the enhancements of the signal-to-noise ratio with the low pass filter only (Figure 4c) and with the connecting box only (Figure 4b). The combination of the two in Figure 4d leads to a significant increase in the signal-to-noise ratio (10.0 compared to around 5.5 for the connecting box only and 5.1 for the filter only).

2.6 Temperature control

A Bruker Cooling Unit I was used with nitrogen gas cooled down by circulating in a liquid nitrogen bath. The temperature is measured by a thermocouple at the bottom of the holder and regulated by controlling the nitrogen flow and a small heating resistance at the top of the glass dewar.

2.7 Galvanostatic charging of the electrochemical cell

A VSP 200 Biologic cycler with the EC lab software was used during the whole study. The cell was charged in galvanostatic mode with a constant current I, defined in the community from the full expected charge C: $I=C/T_{charge(hours)}$. A current of C/10 means charging the cell with the current that should bring the battery from empty to full charge in 10 hours. We used the areal capacity of the graphite electrode (as provided by the supplier) and the current densities are reported using the real area of the graphite electrode (see paragraph 2.2).

The initial “formation” of the cell was performed at room temperature and is composed of 2 cycles of charge and discharge between 2.7 V and 4.2 V at a C/10 current (392 µA/cm^2) followed by 2 cycles at a C/5 current (expected full charge in 5 hours: 784 µA/cm^2). Each charge during formation was ended by a constant voltage (CV) step at 4.2 V which stopped when the current dropped below a threshold: here, C/50 current (78 µA/cm^2): the current that would be used to fully charge an empty battery in 50 h. We obtained a formation capacity (capacity of 4th charge) of 2.95 mAh/cm², which is not as good as the constructor data (3.52 mAh/cm^2), but deemed sufficient for this proof of concept.

Charge-discharge cycles 5 to 10 were performed in the NMR probe inside the NMR magnet, at a temperature of 0°C and at a constant current amounting to 2C (a charge from empty to expected capacity in ½ h: 7.84 mA/cm^2) until reaching a potential of 4.2 V. This limit is defined to reduce electrolyte decomposition, another degradation phenomenon in batteries. As in the formation cycles, the voltage was maintained at this maximum voltage during a constant-voltage step (CV), except for cycle 5, to enable kinetically-limited redox reactions to proceed further and reach the best available stored capacity. Discharge was performed at a lower current (D/2, theoretical full discharge in 2 h: 1.96 mA/cm^2) to avoid battery degradation and to decorrelate limitations from fast discharge and fast charge.

Cycles 11 to 20 were performed with the battery in the NMR probe placed outside of the magnet to assess that the battery was still performing reasonably well at room temperature and low currents (charge in 10 h, discharge in 10 h: 392 µA/cm^2). These cycles were performed in the NMR probe placed out of the NMR magnet for reducing the NMR spectrometer use.

Table S1 in SI provides the capacities in charge (at the end of the CV step) and discharge, as well as coulombic efficiencies and capacity ratio for readers interested in the detailed electrochemical performance of the battery.

2.8 NMR spectroscopy acquisition

1316 single-pulse ^{7}Li NMR spectra were recorded one after the other during the whole *operando* experiment (except in the middle of the 8th cycle), for a recording duration of 23.8 hours. The measurements were performed on a Bruker Avance III 4.7 T spectrometer with a modified SOL Bruker probe. Each spectrum was obtained by co-addition of 256 transients to increase the signal to noise ratio, for a total duration of 65 s per spectrum. A one-pulse NMR sequence is used; with a square pulse followed by a dead time of 12 µs and free induction decay sampling for 82 ms (spectral window of 50 kHz). The RF excitation pulse was a square 18.2 µs pulse at 50 W (13.7 kHz), determined prior to the *operando* measurement on an aqueous solution of 1 mol.L^{-1} lithium chloride used as a reference. The carrier frequency was always set next to the electrolyte signal (~1 ppm).
A short interscan delay of 0.172 s was used to optimize the signal-to-noise ratio for metallic lithium, as we focus on the onset of plating. As most of the components in the battery have slower longitudinal relaxation, all ^{7}Li peaks were partially saturated and quantitative conditions were not met.

2.9 NMR data processing

The NMR data consist of a series of 1D 7Li NMR spectra. Each ^{7}Li NMR spectrum was zero-filled to 16384 points and apodized before Fourier transform in Topspin. An exponential apodization (Bruker exponential apodization parameter LB of 50 Hz) was applied on all the spectra to enhance the signal-to-noise ratio without unnecessary line broadening for the signals of interest.
The first order phase correction parameter phc1 in Topspin was set based on the dead time de, the dwell time dw and the pulse length p1 using the formulae that gave empirically the best results in our more general experience (most probably an effect of the proprietary digital filters applied by Topspin):

$$phc1 = -\frac{360}{dw} \cdot (de + 0.36 \cdot p1)$$

The spectra were then loaded directly in MATLAB (version R2017b, The Mathworks, Inc) using a set of matNMR [52] routines. Baseline distortion, due to the probe dead time and potentially probe ringing, must be removed before integration of the metallic Li range. In addition, the broad contribution from NMC622 appears in the baseline of the spectrum, is too broad for proper fitting, and evolves with the state-of-charge of the electrode. Baseline correction tools, such as *MY-Baseline-Corrector* [53], could not be used here. The NMC broad contribution indeed perturbs the automatic determination of the "baseline range" and the "signal range" in *MY-Baseline-Corrector* and will induce spectrum-dependent variations in the areas that may hide small (but real) trends in the metallic lithium range. Instead, we chose to perform a 3rd order polynomial fit of the "baseline" in MATLAB, using the regions considered without exploitable signal (-65 ppm to -30 ppm, 60 ppm to 260 ppm, and 330 ppm to 580 ppm). The polynomial coefficients are plotted as a function of spectrum number in Figure S3. Variations in the coefficients are principally a signature of the changes in the positive

electrode, even though the intensities should be commented carefully due to the partial saturation of the signal.

2.10 Integration of spectra and uncertainty

A homemade MATLAB code was then used to correlate the electrochemistry data with the NMR processed data. An NMR timeline was created from the NMR data.
The electrochemical data (current, voltage, differential capacity as a function of time) were exported from EC-LAB (Biologic) as text and imported in MATLAB. They were re-gridded on the NMR timeline.

Two spectral ranges were integrated, described as “metallic lithium” (260 to 330 ppm) and “other constituents”: -30 to 60 ppm for lithium in graphite (central transition), electrolyte and passivation layers. The results were not smoothed to keep the best time resolution and avoid over-confidence in the treatment of the data.
A detection threshold was defined using the noise maximum amplitude in the region without signal: the onset of Li plating will be considered as certain for metallic lithium areas above that limit. This threshold is rather conservative; it could be optimized by taking into account the integration range, much larger for the residual area compared to the metallic Li area.

3 Results & Discussion

As a proof of concept we study the kinetic limitations of a commercial graphite electrode at fast charging rate and low temperature (0°C). We try to respect as much as possible “real” conditions: commercial positive electrode NMC622, pressure applied to the stacked electrodes thanks to our Kel-F swagelok-type cell container [44], and charging protocol validated in industry. Materials and Methods provide details on the electrodes and electrochemical protocol.

3.1 Electrochemical data

Figure 5 gives insight into the battery evolution with cycles of charge and discharge. It shows the experimental areal capacity (stored charge per unit surface) of the battery as histograms for all the charge-discharge cycles experienced by the battery. The current for the charge is indicated as C/T or D/T on top of the histograms (with T the time needed for a full charge or discharge). Note that the charge capacities are divided in two stacked histograms: the capacity obtained through the initial constant-current step (CC, in pink) and the capacity obtained during the 4.2 V constant-voltage step (CV) at the end of each charge (in yellow). The discharge was made at a lower current, so that no CV step was applied and the areal discharge capacity is a single green histogram for each cycle.

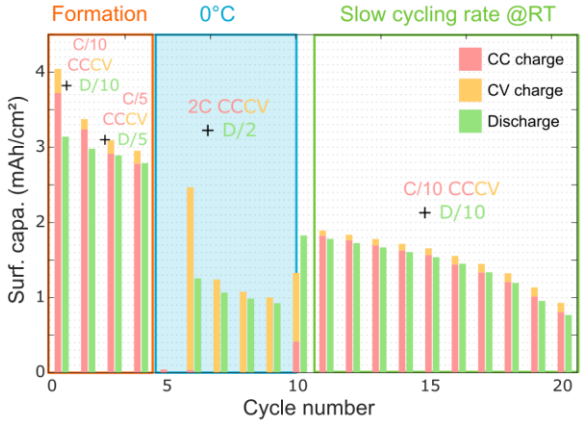

Figure 5: Histograms of areal capacities (stored charge per cm^2) for the 20 cycles of charge-discharge of the battery. The capacities for charge are separated in two contributions: the capacity obtained by constant current charge (CC, pink) and the extra capacity obtained by holding the voltage at 4.2 V (CV, yellow). The discharge capacity appears in green. Cycles 5 to 10 are performed at 0°C in the operando NMR setup. Cycles 11 to 20 are performed at room temperature in the NMR probe but out of the NMR magnet (optimization of spectrometer time).

In **Figure 5** the four initial charge-discharge cycles are used as a "formation" step to stabilize the battery capacity (detailed descriptions in Materials & Methods). In this step, irreversible capacity loss is mainly due to the formation of solid electrolyte interphases (SEI) on the graphite electrode.

The following cycles (5 to 10) were performed in the *operando* NMR setup to study kinetic limitations in the battery. Two conditions known to favour Li plating at the negative electrode were used: high currents (current for a full charge in ½ h) and low temperature (0°C). Discharge was performed at a lower current to avoid additional battery degradation and to decorrelate fast discharge effects from fast charge limitations.
A drastic loss of capacity was observed for the charges and discharges in these cycles, with capacities reduced to 34%-42% of the experimental capacity at the end of formation (cycle 4). Coulombic efficiencies (energy retrieved on discharge versus energy provided on charge) remained however good (table S1 in SI). This behaviour hints at an increased polarization of the cell, as expected for low temperature and faster charge. The cut-off voltage of 4.2 V was indeed reached in less than 30 s and the constant current (CC) step amounted to almost no capacity storage at high currents. The constant-voltage (CV) step is an absolute requirement to store capacity in the cell when charging fast. This is obvious in the 5th cycle, for which no CV step was applied: the battery reaches the upper cut-off voltage due to strong polarization and no energy is available for discharge.
Upon further charges-discharges performed at room temperature and low charging rates (cycles 11-20), a better capacity was partially recovered but a constant degradation of the battery performance was observed afterwards.

3.2 *Operando* ^{7}Li NMR spectroscopy

Operando ^{7}Li NMR one-pulse spectra were acquired and analyzed to detect Li plating for the whole duration of the charge-discharge cycles 5 to 10 of the battery in the *operando* NMR setup, at a temperature of 0°C and using a fast charging rate (current for a full charge in ½ h). The electrochemical data were recorded simultaneously (voltage, current, capacity).

As we focus on the detection of the onset of plating, we aimed at increasing our sensitivity, without trying to be fully quantitative. This was attained by using an optimized interscan delay to increase the signal-to-noise without decreasing the time resolution (more scans per minute). As most of the components in the battery have slower longitudinal relaxation compared to that of metallic bulk Li (150 ms on our 4.7 T), all ^{7}Li peaks were partially saturated and quantitative conditions were not met. A repetition time above 30 s would be necessary to ensure that the measured spectra of all lithiated phases are quantitative. The loss of time resolution, even with an Ernst angle approach as proposed by Lorie Lopez *et al.* [27], would be prohibitive for detecting the onset of metallic Li.

Another challenge consisted in the broad contribution of the positive paramagnetic electrode. The ^{7}Li NMR spectrum of $LiNi_{0.6}Mn_{0.2}Co_{0.2}O_2$ (NMC622) is much broader than NMC811 [35], so that it appears as a "baseline distortion", which varies as the redox state of NMC622 is modified upon charge-discharge. The conductivity of the sample also changes as the battery is cycled, resulting in slight changes in the tuning of the probe and eventually the phase of the spectra. We relied on using a fixed 1st order phase correction calculated based on the deadtime of the probe, and we fitted the "baseline" as a whole using a third order polynomial in MATLAB (details in Materials and Methods).

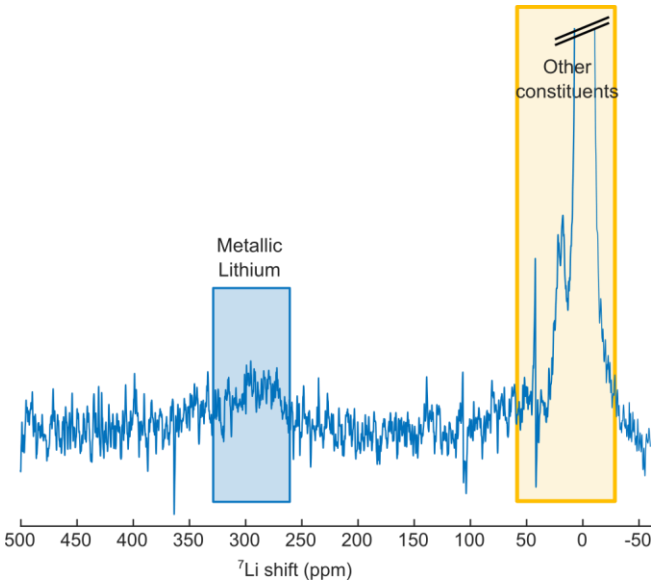

Figure 6: Typical spectrum after processing and "baseline" fit, showing the integration zones

After processing, the *operando* NMR data consist of a series of 1D ^{7}Li NMR spectra, correlated to the electrochemical data of the battery. Figure 6 shows a spectrum extracted from the data after complete processing and indicates the two integration areas used in the following: metallic lithium from 260 to 330 ppm and other constituents (lithiated graphite, lithiated

compounds in the solid-electrolyte interface, lithium ions in the liquid electrolyte…) from -30 to 60 ppm.

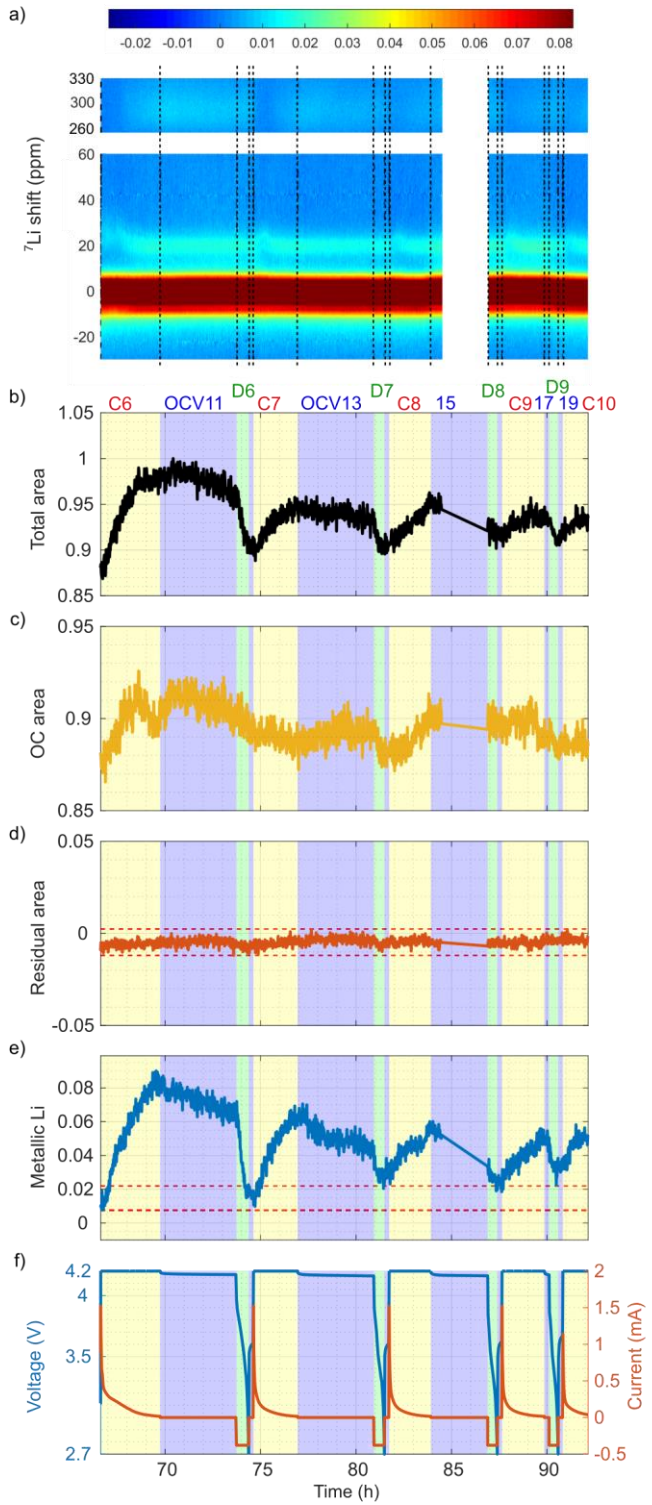

Figure 7: *Operando* NMR characterization of the cell from 6th to 10th charge - discharge. a) Series of ^{7}Li spectra (vertical) as a function of time (horizontal), shown as contour plot; b) Evolution of the total area of spectrum with time; c) Absolute area of other constituents (OC, yellow) ; d) Absolute area of the residual noise, used for uncertainty assessment; e) Absolute area of metallic lithium (blue) ; d) Voltage (blue) and current profile (in red). The

green background corresponds to discharges, the pink and yellow backgrounds indicate CC and CV charging steps, respectively. The blue background shows open circuit voltage steps. The red dashed line represents the uncertainty. Data are reported against time (with the origin at the beginning of the first formation cycle).

Figure *7* correlates the electrochemical data in f) to the *operando* ^{7}Li NMR characterization during the low temperature experiment from 6th charge to 10th charge. Every spectrum is the signature of the environment of the ^{7}Li atoms in the battery averaged over 65 s and more than a thousand spectra were recorded in a row.
Figure 7f shows the voltage and current intensity for cycles 6-10. These profiles do not display any obvious malfunction of the cell. The 4.2V cut-off is reached in less than 30 s for fast charge at low temperature, due to the large polarization of the battery cell.

The contour plot of the evolution of the NMR spectra is shown as a function of time in **Figure 7a**. Metallic lithium appears in the 260-330 ppm region of the spectrum. The other lithium-containing species (OC, for other constituents) appear in the -30 to 60 ppm region. Notably, this region contains signals from lithium ions in the electrolyte, lithiated graphite (central transition), lithium-containing decomposition products (solid-electrolyte interphases - SEI). Note that the recording conditions are not quantitative, so that intensities of the various components are weighted down owing to their longitudinal relaxation, which changes depending on the state of charge.

As shown in **Figure 7b** the full spectrum area is varying with time, even after the baseline fit. These changes are expected, as the repetition time is too short to be quantitative: a decrease in the longitudinal relaxation rate T_1 of the components results in an increase of the experimental areas at fixed repetition time and vice versa.

Figure 7c indicates that most of the signal (>85%) is contained in the -30 to 60 ppm region (OC, other components). Even though the measurements are not quantitative, we can still qualitatively observe the lithiation and delithiation mechanisms of the graphite through the satellite peaks near 30 ppm.
An additional experiment (Part 4 in SI) indicates that a slightly longer repetition time enables better following the lithiation and delithiation stages of graphite with the area. The longitudinal relaxation time T_1 is indeed shorter for the concentrated stages, so that the increased signal from the larger amount of Li in graphite adds up with a better relaxation of the signal between transients. The repetition time has therefore to be chosen to strike a balance between the materials of interest in the battery and the time resolution/detection limit.

Turning now to our initial goal, we concentrate on the integration of the metallic Li range in the ^{7}Li spectra acquired with the shortest repetition time to identify the onset of metallic Li plating as early as possible. In **Figure 7e,** as expected, the abusive conditions - fast charge combined with low temperature - result in metallic Li plating. It is detected at the beginning of the CV step (yellow) in charge, for each cycle. Even though the conditions are optimized to enhance the proportion of metallic lithium detection over the other components, the metallic lithium peak amounts to less than 10% of the maximum total ^{7}Li signal.

In order to determine the onset of lithium plating, we estimated the uncertainty on the integrated areas. We consider that the main source of error on the integrated area originates from the "baseline" fit. The residual area (**Figure 7d**) was obtained by integration of the regions considered without signal after the "baseline" fit (330 to 579 ppm, 60 to 260 ppm, -65 to -30 ppm). The maximum amplitude of this residual area over the 1316 *operando* spectra was used as our detection threshold for this battery. The criterion for stating (with good confidence) that Li plating occurred was therefore defined as follows: the area for the 260-330 ppm region should be higher than this threshold (2.2% of the maximum total area for the battery in this report). It appears as a red dashed line in **Figure *7***. Note that this detection threshold is rather conservative and could be improved by taking into account the integration range, much larger for the residual area compared to the metallic Li area.

All cycles 6 to 10 show a similar behaviour, with metallic lithium deposition during charge and stripping/change in morphology during discharge. Interestingly, the maximum amount of metallic lithium detected in charge decreases with the cycle number, either because less Li is plated or because the morphology changes the relationship between the NMR area and the amount of metal.

3.3 Linking onset of Li plating (as determined by NMR) and electrochemical data

This approach enables the determination of the electrochemical descriptors of the battery as close as possible to the onset of Li plating. The current in the constant-voltage step (CV) measured at the onset of Li plating is given in **Table 2** for each cycle. In CV steps, the current decreases from its initial value (the value used in the previous constant-current step, 1.518 A) until all reactions that were kinetically hindered have taken place.

Cycle steps	Capacity of step ($mAh \cdot cm^{-2}$)	Capacity retention $Q_{(n)}/Q_{(4)}$	Discharge coulombic efficiency (Q_{Dn}/Q_{Cn})	Charge coulombic efficiency (Q_{Cn}/Q_{Dn-1})	Current (for CC charge or discharge)	Current and Voltage at onset of plating	Metallic ^7Li area at end of steps Expressed as % of total Li signal at that time
C6 +CV *	2,47	84%		88%	2C (1.52 mA)	0.27 mA 4.2 V	8.4
OCV11 *		-					6.0
D6 *	1,26	43%	51%		D/2 (0.38 mA)	Li consumed	(1.9)
OCV12*		-					(1.2)
C7+CV *	1,24	42%		98%	2C	0.15 mA 4.2 V	6.8
OCV13*		-					4.8
D7 *	1,07	36%	86%		D/2-	Li remains	2.8
OCV14*		-					3.2
C8+CV *	1,08	37%		101%	2C	Li remains	5.9
OCV15 *		-					3.7
D8 *	0,99	34%	92%		D/2	Li consumed	2.3

OCV16*		-				2.6
C9+CV *	1,00	34%		101%	2C	0.34 mA 4.2 V	5.4
OCV17*		-				5.4
D9 *	0,93	32%	93%		D/2	Li remains	3.6
OCV18*		-				3.9
C10+CV *	1,33	45%		143%	2C	Li remains	5.5

Table 2: Overview of cycling steps and information about appearance and evolution of relative areas of metallic lithium from cycle #6 to charge #10. The detection threshold for metallic Li is 2.2% of the maximum total area (mainly partially saturated graphitic compounds).

In cycle 6 the current decreased to 18% of its initial value during the CV step before the onset of Li plating. In cycle 7, plating set for an even lower current (10% of the initial current). We do not observe a clear correlation between the current at the onset of plating and the coulombic efficiency or the capacity retention. More data will be necessary to extract meaningful trends, but this interesting behaviour will be further explored in the future.

In the following we comment on the evolution of the area of detected metallic Li signal, assuming that no drastic change in the morphology or conductivity of metallic Li happen. Knowing that this assumption has to be confirmed in the future, we provide hypotheses for the evolutions. As can be seen in **Figure 7e**, the amount of metallic Li increases during charge and decreases upon discharge. The discharges of cycles 6-10 reuse part of the plated Li but, even at low currents, they do not oxidize completely the Li deposit, so that after the 7th charge metallic Li signal remains detected at all times. Metallic lithium particles remaining at the end of each discharge probably react with the electrolyte to form inactive ("dead") lithium embedded in a passivation layer. Interestingly, the maximum detected amount of metallic Li in the CV step does not increase with cycle number. This could be related to a varying morphology of the metallic Li deposit or a change in the overpotentials leading to less metallic Li deposition.

The open-circuit voltage steps (OCV, blue blocks in **Figure 7**), performed at the end of each charge, reveal an evolution in the detected area of metallic lithium. It may indicate that plated lithium is available for chemical reaction and can react with the electrolyte to form passivation layers or with the surface of the graphite electrode to form lithiated graphite as seen by Sanders *et al.* at room temperature [33]. No electrochemical-driven reaction can occur, as no current is passed through the electrodes in open-circuit.

Interestingly, the assessment of the battery after stopping the abusive conditions (low-temperature, fast-charge cycling) demonstrated a recovery of 62% of the capacity initially obtained at the end of the 4th charge (formation step), while the capacity was only 32% (of that in the last formation step) at 0°C and at a high charging current (**Figure 5**). We therefore assume that the battery behaviour at 0°C was reasonably representative of a commercial battery in similar conditions. However, from cycle 10 to 20 the coulombic efficiencies and the reversible capacities decreased drastically (Table S1 in SI). We assign that irreversible capacity

either to the continuing formation of dead lithium along time, with formation of a passivation layer, or to other side reactions, for example on the positive electrode.
The above degradation hypotheses should be validated using a larger ensemble of cells for reducing the error, to draw final conclusions from robust statistics. This is out of the scope of the present proof-of-concept; it will be the subject of future studies.

4 Conclusion

As a conclusion, we showed that *operando* NMR characterization could be tuned to detect the onset of small metallic lithium deposits during electrochemical cycling of a full cell with industry-grade electrodes and control over the pressure applied to the electrodes. We developed a new *operando* NMR setup for low temperature experiments, with special emphasis on increasing the limit of detection. We adapted a probe to our already-functional Kel-F cells (Swagelok-type) with the development of a cell holder and optimized the cabling setup for robustness and to attenuate the induced electric noise.
This setup, applied to the *operando* ^{7}Li NMR characterization of a NMC622/Graphite cell fast-charged at 0°C, was able to detect lithium plating and to follow the evolution of the detected metallic Li area in open circuit conditions and subsequent discharge. Several observations were reported that call for further studies, using large sets of cells to obtain statistical results, ideally using commercial cells. A partial stripping upon discharge was reported and suggests that dead lithium is formed. Interestingly, the amount of detected metallic lithium during CV did not increase with cycle number. The evolution of the detected amount of deposited lithium under open circuit conditions, assigned to reaction with graphite or SEI formation, should also be analyzed further in the future. Dead lithium or other side reactions could be related to the fast decay in capacity observed upon cycling after bringing the cell back to room temperature.

This approach extends the toolkit available for *operando* NMR characterization of electrochemical devices to low temperature and fast charge, with a relative control on pressure. We hope that this report will raise the interest of the community and will pave the way to robust and detailed studies of Li-ion batteries, towards a better understanding of the parameters responsible for lithium plating and improvement of the charging protocols at low temperature for commercial cells.

5 Ackowledgments

P. Melin, P. Riffard, W. Hate and P. Casero are acknowledged for their support and useful discussions. Financial support for LAdA by the Association Nationale de la Recherche et de la Technologie (ANRT, France) is gratefully acknowledged. The authors aknowledge support from the Agence Nationale de la Recherche (ANR) with the LABEX STORE-EX (ANR-10-LABX-76), from the Centre National de la Recherche Scientifique (CNRS) and from Université d'Orléans.

6 References

[1] C.R. Birkl, M.R. Roberts, E. McTurk, P.G. Bruce, D.A. Howey, Degradation diagnostics for lithium ion cells, Journal of Power Sources. 341 (2017) 373–386. https://doi.org/10.1016/j.jpowsour.2016.12.011.
[2] M.M. Kabir, D.E. Demirocak, Degradation mechanisms in Li-ion batteries: a state-of-the-art review: Degradation Mechanisms in Li-ion Batteries: A State-of-the-Art Review, International Journal of Energy Research. 41 (2017) 1963–1986. https://doi.org/10.1002/er.3762.
[3] M.R. Palacín, Understanding ageing in Li-ion batteries: a chemical issue, Chem. Soc. Rev. 47 (2018) 4924–4933. https://doi.org/10.1039/C7CS00889A.
[4] J.P. Pender, G. Jha, D.H. Youn, J.M. Ziegler, I. Andoni, E.J. Choi, A. Heller, B.S. Dunn, P.S. Weiss, R.M. Penner, C.B. Mullins, Electrode Degradation in Lithium-Ion Batteries, ACS Nano. (2020) acsnano.9b04365. https://doi.org/10.1021/acsnano.9b04365.
[5] E.J. Dufek, D.P. Abraham, I. Bloom, B.-R. Chen, P.R. Chinnam, A.M. Colclasure, K.L. Gering, M. Keyser, S. Kim, W. Mai, D.C. Robertson, M.-T.F. Rodrigues, K. Smith, T.R. Tanim, F.L.E. Usseglio-Viretta, P.J. Weddle, Developing extreme fast charge battery protocols – A review spanning materials to systems, Journal of Power Sources. 526 (2022) 231129. https://doi.org/10.1016/j.jpowsour.2022.231129.
[6] T. Waldmann, B.-I. Hogg, M. Wohlfahrt-Mehrens, Li plating as unwanted side reaction in commercial Li-ion cells – A review, Journal of Power Sources. 384 (2018) 107–124. https://doi.org/10.1016/j.jpowsour.2018.02.063.
[7] S.S. Zhang, The effect of the charging protocol on the cycle life of a Li-ion battery, Journal of Power Sources. 161 (2006) 1385–1391. https://doi.org/10.1016/j.jpowsour.2006.06.040.
[8] Q. Liu, C. Du, B. Shen, P. Zuo, X. Cheng, Y. Ma, G. Yin, Y. Gao, Understanding undesirable anode lithium plating issues in lithium-ion batteries, RSC Adv. 6 (2016) 88683–88700. https://doi.org/10.1039/C6RA19482F.
[9] M. Woody, M. Arbabzadeh, G.M. Lewis, G.A. Keoleian, A. Stefanopoulou, Strategies to limit degradation and maximize Li-ion battery service lifetime - Critical review and guidance for stakeholders, Journal of Energy Storage. 28 (2020) 101231. https://doi.org/10.1016/j.est.2020.101231.
[10] N. Wassiliadis, J. Schneider, A. Frank, L. Wildfeuer, X. Lin, A. Jossen, M. Lienkamp, Review of fast charging strategies for lithium-ion battery systems and their applicability for battery electric vehicles, Journal of Energy Storage. 44 (2021) 103306. https://doi.org/10.1016/j.est.2021.103306.
[11] U. Janakiraman, T.R. Garrick, M.E. Fortier, Review—Lithium Plating Detection Methods in Li-Ion Batteries, J. Electrochem. Soc. 167 (2020) 160552. https://doi.org/10.1149/1945-7111/abd3b8.
[12] P.P. Paul, E.J. McShane, A.M. Colclasure, N. Balsara, D.E. Brown, C. Cao, B.-R. Chen, P.R. Chinnam, Y. Cui, E.J. Dufek, D.P. Finegan, S. Gillard, W. Huang, Z.M. Konz, R. Kostecki, F. Liu, S. Lubner, R. Prasher, M.B. Preefer, J. Qian, M.-T.F. Rodrigues, M. Schnabel, S.-B. Son, V. Srinivasan, H.-G. Steinrück, T.R. Tanim, M.F. Toney, W. Tong, F. Usseglio-Viretta, J. Wan, M. Yusuf, B.D. McCloskey, J. Nelson Weker, A Review of Existing and Emerging Methods for Lithium Detection and Characterization in Li-Ion and Li-Metal Batteries, Advanced Energy Materials. 11 (2021) 2100372. https://doi.org/10.1002/aenm.202100372.

[13] T. Foroozan, S. Sharifi-Asl, R. Shahbazian-Yassar, Mechanistic understanding of Li dendrites growth by in- situ/operando imaging techniques, Journal of Power Sources. 461 (2020) 228135. https://doi.org/10.1016/j.jpowsour.2020.228135.
[14] H. Li, S. Guo, H. Zhou, In-situ/operando characterization techniques in lithium-ion batteries and beyond, Journal of Energy Chemistry. 59 (2021) 191–211. https://doi.org/10.1016/j.jechem.2020.11.020.
[15] F. Blanc, M. Leskes, C.P. Grey, In Situ Solid-State NMR Spectroscopy of Electrochemical Cells: Batteries, Supercapacitors, and Fuel Cells, Acc. Chem. Res. (2013). https://doi.org/10.1021/ar400022u.
[16] O. Pecher, J. Carretero-González, K.J. Griffith, C.P. Grey, Materials' Methods: NMR in Battery Research, Chem. Mater. 29 (2017) 213–242. https://doi.org/10.1021/acs.chemmater.6b03183.
[17] J.Z. Hu, N.R. Jaegers, M.Y. Hu, K.T. Mueller, In situ and ex situ NMR for battery research, Journal of Physics: Condensed Matter. 30 (2018) 463001. https://doi.org/10.1088/1361-648X/aae5b8.
[18] K. Gotoh, T. Yamakami, I. Nishimura, H. Kometani, H. Ando, K. Hashi, T. Shimizu, H. Ishida, Mechanisms for overcharging of carbon electrodes in lithium-ion/sodium-ion batteries analysed by operando solid-state NMR, J. Mater. Chem. A. 8 (2020) 14472–14481. https://doi.org/10.1039/D0TA04005C.
[19] S. Krachkovskiy, M.L. Trudeau, K. Zaghib, Application of Magnetic Resonance Techniques to the In Situ Characterization of Li-Ion Batteries: A Review, Materials. 13 (2020) 1694. https://doi.org/10.3390/ma13071694.
[20] X. Liu, Z. Liang, Y. Xiang, M. Lin, Q. Li, Z. Liu, G. Zhong, R. Fu, Y. Yang, Solid-State NMR and MRI Spectroscopy for Li/Na Batteries: Materials, Interface, and In Situ Characterization, Advanced Materials. 33 (2021) 2005878. https://doi.org/10.1002/adma.202005878.
[21] K. Bagheri, M. Deschamps, E. Salager, Nuclear magnetic resonance for interfaces in rechargeable batteries, Current Opinion in Colloid & Interface Science. 64 (2023) 101675. https://doi.org/10.1016/j.cocis.2022.101675.
[22] R.E. Gerald II, J. Sanchez, C.S. Johnson, R.J. Klingler, J.W. Rathke, In situ nuclear magnetic resonance investigations of lithium ions in carbon electrode materials using a novel detector, J. Phys.: Condens. Matter. 13 (2001) 8269.
[23] F. Chevallier, M. Letellier, M. Morcrette, J.-M. Tarascon, E. Frackowiak, J.-N. Rouzaud, F. Béguin, In Situ 7Li-Nuclear Magnetic Resonance Observation of Reversible Lithium Insertion into Disordered Carbons, Electrochemical and Solid-State Letters. 6 (2003) A225. https://doi.org/10.1149/1.1612011.
[24] B. Key, R. Bhattacharyya, M. Morcrette, V. Seznéc, J.-M. Tarascon, C.P. Grey, Real-Time NMR Investigations of Structural Changes in Silicon Electrodes for Lithium-Ion Batteries, J. Am. Chem. Soc. 131 (2009) 9239–9249. https://doi.org/10.1021/ja8086278.
[25] R. Bhattacharyya, B. Key, H. Chen, A.S. Best, A.F. Hollenkamp, C.P. Grey, In situ NMR observation of the formation of metallic lithium microstructures in lithium batteries, Nature Mater. 9 (2010) 504–510. https://doi.org/10.1038/nmat2764.
[26] S.A. Krachkovskiy, J.M. Foster, J.D. Bazak, B.J. Balcom, G.R. Goward, Operando Mapping of Li Concentration Profiles and Phase Transformations in Graphite Electrodes by Magnetic Resonance Imaging and Nuclear Magnetic Resonance Spectroscopy, J. Phys. Chem. C. 122 (2018) 21784–21791. https://doi.org/10.1021/acs.jpcc.8b06563.

[27] J.L.L. Lopez, P. J. Grandinetti, A. C. Co, Enhancing the real-time detection of phase changes in lithium–graphite intercalated compounds through derivative operando (dOp) NMR cyclic voltammetry, Journal of Materials Chemistry A. 6 (2018) 231–243. https://doi.org/10.1039/C7TA07521A.
[28] S.A. Kayser, A. Mester, A. Mertens, P. Jakes, R.-A. Eichel, J. Granwehr, Long-run in operando NMR to investigate the evolution and degradation of battery cells, Phys. Chem. Chem. Phys. 20 (2018) 13765–13776. https://doi.org/10.1039/C8CP01067F.
[29] K. Gotoh, M. Izuka, J. Arai, Y. Okada, T. Sugiyama, K. Takeda, H. Ishida, In situ 7Li nuclear magnetic resonance study of the relaxation effect in practical lithium ion batteries, Carbon. 79 (2014) 380–387. https://doi.org/10.1016/j.carbon.2014.07.080.
[30] J. Arai, Y. Okada, T. Sugiyama, M. Izuka, K. Gotoh, K. Takeda, In Situ Solid State 7Li NMR Observation of Lithium Metal Deposition during Overcharge in Lithium Ion Battery, Journal of the Electrochemical Society. 162 (2015) A952–A958. https://doi.org/10.1149/2.0411506jes.
[31] A.R. Aguilera, B. MacMillan, S. Krachkovskiy, K.J. Sanders, F. Alkhayri, C. Adam Dyker, G.R. Goward, B.J. Balcom, A parallel-plate RF probe and battery cartridge for 7Li ion battery studies, Journal of Magnetic Resonance. 325 (2021) 106943. https://doi.org/10.1016/j.jmr.2021.106943.
[32] S.A. Krachkovskiy, M. Reza, A.R. Aguilera, I.C. Halalay, B.J. Balcom, G.R. Goward, Real-Time Quantitative Detection of Lithium Plating by In Situ NMR Using a Parallel-Plate Resonator, J. Electrochem. Soc. 167 (2020) 130514. https://doi.org/10.1149/1945-7111/abb7ea.
[33] K.J. Sanders, A.R. Aguilera, J.R. Keffer, B.J. Balcom, I.C. Halalay, G.R. Goward, Transient lithium metal plating on graphite: Operando 7Li nuclear magnetic resonance investigation of a battery cell using a novel RF probe, Carbon. 189 (2022) 377–385. https://doi.org/10.1016/j.carbon.2021.12.082.
[34] J. Arai, R. Nakahigashi, Study of Li Metal Deposition in Lithium Ion Battery during Low-Temperature Cycle Using In Situ Solid-State 7Li Nuclear Magnetic Resonance, J. Electrochem. Soc. 164 (2017) A3403. https://doi.org/10.1149/2.1921713jes.
[35] K. Märker, C. Xu, C.P. Grey, Operando NMR of NMC811/Graphite Lithium-Ion Batteries: Structure, Dynamics, and Lithium Metal Deposition, J. Am. Chem. Soc. 142 (2020) 17447–17456. https://doi.org/10.1021/jacs.0c06727.
[36] H.J. Chang, N.M. Trease, A.J. Ilott, D. Zeng, L.-S. Du, A. Jerschow, C.P. Grey, Investigating Li Microstructure Formation on Li Anodes for Lithium Batteries by in Situ 6Li/7Li NMR and SEM, J. Phys. Chem. C. 119 (2015) 16443–16451. https://doi.org/10.1021/acs.jpcc.5b03396.
[37] V. Küpers, M. Kolek, P. Bieker, M. Winter, G. Brunklaus, In situ 7 Li-NMR analysis of lithium metal surface deposits with varying electrolyte compositions and concentrations, Physical Chemistry Chemical Physics. 21 (2019) 26084–26094. https://doi.org/10.1039/C9CP05334D.
[38] G. Fuchs, L. Willenberg, F. Ringbeck, D.U. Sauer, Post-Mortem Analysis of Inhomogeneous Induced Pressure on Commercial Lithium-Ion Pouch Cells and Their Effects, Sustainability. 11 (2019) 6738. https://doi.org/10.3390/su11236738.
[39] A.J. Ilott, M. Mohammadi, H.J. Chang, C.P. Grey, A. Jerschow, Real-time 3D imaging of microstructure growth in battery cells using indirect MRI, Proceedings of the National Academy of Sciences. 113 (2016) 10779–10784. https://doi.org/10.1073/pnas.1607903113.

[40] M. Mohammadi, A. Jerschow, In situ and operando magnetic resonance imaging of electrochemical cells: A perspective, Journal of Magnetic Resonance. 308 (2019) 106600. https://doi.org/10.1016/j.jmr.2019.106600.
[41] S. Benders, M. Mohammadi, M.J. Ganter, C.A. Klug, A. Jerschow, Mapping oscillating magnetic fields around rechargeable batteries, Journal of Magnetic Resonance. 319 (2020) 106811. https://doi.org/10.1016/j.jmr.2020.106811.
[42] B.J. Walder, M.S. Conradi, J.J. Borchardt, L.C. Merrill, E.G. Sorte, E.J. Deichmann, T.M. Anderson, T.M. Alam, K.L. Harrison, NMR spectroscopy of coin cell batteries with metal casings, Science Advances. 7 (2021) eabg8298. https://doi.org/10.1126/sciadv.abg8298.
[43] E. Salager, In Situ Spectroscopic Imaging of Devices for Electrochemical Storage with Focus on the Solid Components, in: Magnetic Resonance Microscopy, John Wiley & Sons, Ltd, 2022: pp. 355–381. https://doi.org/10.1002/9783527827244.ch16.
[44] E. Salager, V. Sarou-Kanian, M. Sathiya, M. Tang, J.-B. Leriche, P. Melin, Z. Wang, H. Vezin, C. Bessada, M. Deschamps, J.-M. Tarascon, Solid-State NMR of the Family of Positive Electrode Materials Li2Ru1–ySnyO3 for Lithium-Ion Batteries, Chem. Mater. 26 (2014) 7009–7019. https://doi.org/10.1021/cm503280s.
[45] J.A. Tang, S. Dugar, G. Zhong, N.S. Dalal, J.P. Zheng, Y. Yang, R. Fu, Non-Destructive Monitoring of Charge-Discharge Cycles on Lithium Ion Batteries using 7Li Stray-Field Imaging, Sci. Rep. 3 (2013). https://doi.org/10.1038/srep02596.
[46] J.D. Jackson, Classical Electrodynamics Third Edition, 3rd edition, Wiley, New York, 1998.
[47] J.Z. Hu, Z. Zhao, M.Y. Hu, J. Feng, X. Deng, X. Chen, W. Xu, J. Liu, J.-G. Zhang, In situ 7Li and 133Cs nuclear magnetic resonance investigations on the role of Cs+ additive in lithium-metal deposition process, Journal of Power Sources. 304 (2016) 51–59. https://doi.org/10.1016/j.jpowsour.2015.10.067.
[48] J. Mispelter, M. Lupu, Homogeneous resonators for magnetic resonance: A review, Comptes Rendus Chimie. 11 (2008) 340–355. https://doi.org/10.1016/j.crci.2007.10.003.
[49] M. Tang, V. Sarou-Kanian, P. Melin, J.-B. Leriche, M. Ménétrier, J.-M. Tarascon, M. Deschamps, E. Salager, Following lithiation fronts in paramagnetic electrodes with in situ magnetic resonance spectroscopic imaging, Nat Commun. 7 (2016) 13284. https://doi.org/10.1038/ncomms13284.
[50] L.C. Loaiza, E. Salager, N. Louvain, A. Boulaoued, A. Iadecola, P. Johansson, L. Stievano, V. Seznec, L. Monconduit, Understanding the lithiation/delithiation mechanism of Si 1−x Ge x alloys, J. Mater. Chem. A. 5 (2017) 12462–12473. https://doi.org/10.1039/C7TA02100C.
[51] G. Oukali, E. Salager, M.R. Ammar, C.-E. Dutoit, V. Sarou-Kanian, P. Simon, E. Raymundo-Piñero, M. Deschamps, In Situ Magnetic Resonance Imaging of a Complete Supercapacitor Giving Additional Insight on the Role of Nanopores, ACS Nano. 13 (2019) 12810–12815. https://doi.org/10.1021/acsnano.9b04998.
[52] J.D. van Beek, matNMR: A flexible toolbox for processing, analyzing and visualizing magnetic resonance data in Matlab®, Journal of Magnetic Resonance. 187 (2007) 19–26. https://doi.org/10.1016/j.jmr.2007.03.017.
[53] M. Yon, F. Fayon, D. Massiot, V. Sarou-Kanian, Iterative baseline correction algorithm for dead time truncated one-dimensional solid-state MAS NMR spectra, Solid State

Nuclear Magnetic Resonance. 110 (2020) 101699.
https://doi.org/10.1016/j.ssnmr.2020.101699.